Doubly resonant photonic crystal cavity using merged bound states in the continuum

Rui Ge,[1,*] Xiangmin Liu,[1,*] Xiongshuo Yan,[1] Xianfeng Chen,[1,2,3] and Yuping Chen[1,†]

[1]*State Key Laboratory of Advanced Optical Communication Systems and Networks, School of Physics and Astronomy, Shanghai Jiao Tong University, Shanghai 200240, China*

[2]*Shanghai Research Center for Quantum Sciences, Shanghai 201315, China*

[3]*Collaborative Innovation Center of Light Manipulations and Applications, Shandong Normal University, Jinan 250358, China*

(Received 4 February 2023; revised 15 March 2023; accepted 17 March 2023; published 7 April 2023)

In this work, a doubly resonant photonic crystal (PhC) cavity using the merged bound state in the continuum (BIC) is proposed to obtain a higher second harmonic generation (SHG) efficiency. First, by scanning geometry parameters, the accidental BICs and a band-edge mode outside the light cone can be obtained. Then, as the lattice constant or the thickness of the slab is adjusted, the accidental BICs will merge. A supercell with large and small holes is constructed and the band-edge mode outside the light cone can be matched with the merged BIC mode. Finally, the heterostructure PhC cavity is designed. The merged BIC show a high quality factor of about 2000 for the PhC with finite size. The value is four times larger than the one in isolated BIC (about 500). Consequently, the SHG efficiency of the lattice constant near merged BIC of about 4800% W^{-1} is higher than the one of the isolated BIC (about 1000% W^{-1}). This work is expected to provide guidance to the efficient nonlinear conversion in a small volume.

DOI: 10.1103/PhysRevB.107.165406

I. INTRODUCTION

Bound state in the continuum (BIC) has attracted researchers owing to the property of its ultrahigh quality factor (Q factor) [1]. BIC is the vortex center in the polarization directions of far-field radiation and can be characterized by the topological charge [1]. BIC can be applied in laser [2], high-quality sensor [3], optomechanical crystal [4], nonlinear process [5], and chiral-emission metasurface [6]. By splitting the BICs up, the unidirectional guided resonance can be achieved [7,8]. Utilizing the concept of BIC, the doubly resonant photonic crystal (PhC) cavity can be designed and it shows the improved nonlinear frequency conversion process [9–11]. In a doubly resonant cavity, a BIC mode is matched with a band-edge mode outside the light cone and the generated second-harmonic mode can be collected within a small angle. However, the product of Q factors at the band-edge mode and the BIC mode still show room to improve owing to that a higher Q factor will result in a more efficient nonlinear process.

Recently, researchers started to notice a special kind of BIC called "merged-BIC" [12], which is also defined as the "super-BIC" [13]. The merged BIC is formed by merging multiple BIC modes into one point. The traditional BIC-based device usually suffers from scattering loss, which is caused by the coupling with nearby radiative modes. The strategy of merging BICs into one point can enhance the Q factors of nearby resonances in the same band, which will result in the BIC being robust against inevitable fabrication imperfection [12,14–16]. In addition, researchers subsequently found other merits of the merged BIC resulting from this trait. For example, the radiative Q factor at the merged BIC point is generally much larger than the one at the premerging point or isolated BIC point for a device with finite size [13]. Merged BIC have already been widely applied to the ultralow threshold laser [13], chiral resonator [17,18], and acoustic resonator [19]. Moreover, these devices show an improved quality in comparison to the device that used an isolated BIC mode.

Owing to the large Q factor of the merged BIC in a PhC with finite size, the doubly resonant PhC cavity based on that may show improved nonlinear conversion efficiency. However, it requires that the resonant mode at the second-harmonic frequency must be the merged BIC mode and a band-edge mode at the fundamental frequency must be matched with that. Simultaneously, meeting these conditions is inconvenient. Meanwhile, nonlinear conversion efficiency also depends on the Q factor at fundamental frequency and the nonlinear overlapping factor, which should also be considered. In this paper, we take lithium niobate (LN) PhC as an example to demonstrate that utilizing the supercell constructed by the large and small air holes can achieve these goals. The BIC-based LN photonic devices were already theoretically and experimentally exhibited [20–24] and were proven to be an ideal platform for nonlinear process. In previous works, our group proposed the beam splitter [25], cavity [26,27], logic gate [28], and valley waveguide [29] based on lithium niobate PhC. First, the band property of the proposed PhC supercell is analyzed and the approach for matching a band-edge mode outside the light cone with the merged BIC is introduced. Then a heterostructure PhC cavity is considered. After determining the geometry parameters the device can meet the mode-matching condition. Finally, we

*These authors contributed equally to this work.
†ypchen@sjtu.edu.cn

estimate the SHG efficiency of the device at different lattice constants.

II. MODEL AND THEORY

Before discussing our simulations we must first review the four requirements to design a doubly resonant PhC cavity using an isolated BIC [9]. (1) The fundamental mode must be a band-edge mode outside the light cone. (2) The second-harmonic mode must be a BIC mode at the Γ point. (3) Those modes are either the maximum or the minimum in their bands. (4) The periodic electric field of those modes has a nonzero nonlinear overlapping factor. Next we discuss how to transform the BIC mode into the merged BIC mode.

Now back to our design, the first step is to find an accidental BIC mode that satisfies $f_{\text{acc-BIC}} \approx 2f_{\text{band-edge}}$, where $f_{\text{acc-BIC}}$ and $f_{\text{band-edge}}$ represent the frequencies of the accidental BIC and band-edge mode. It is generally simple to obtain an accidental BIC [1], while the mode-matching requirement is, to some extent, difficult to meet. Here we choose the structure in Fig. 1(a), which is infinitely extended. The air holes are etched in the suspended slab and are arranged in a hexagonal lattice. The material of the slab is chosen as LN, which has outstanding nonlinear properties [23]. The current etching technique for LN has demonstrated 85 degrees sidewall angle of holes [30–32]. The dispersion of the material should be considered [9]. The optical axis of LN is set to the z direction, and consequently, the nonlinear tensor d_{31} (4.3 pm/V [21]) is responsible for the second-harmonic generation process. Moreover, we mainly focus on the transverse electric (TE) band at the fundamental frequency and the transverse magnetic (TM) band at the second-harmonic frequency. Intuitively, once the d_{33} tensor is used the nonlinear conversion efficiency will be higher. However, the merged BIC mode that simultaneously satisfies our requirements is hard to obtain. Detailed simulation results with d_{33} are discussed (see the Supplemental Material [33]). The refractive index tensors are $n_x = 2.2111$, $n_y = 2.2111$, and $n_z = 2.1376$ near 1550 nm and $n_x = 2.2587$, $n_y = 2.2587$, and $n_z = 2.1784$ near 775 nm [34]. After numerous simulations with parameter sweep, the lattice constant is set to $a = 650$ nm and the radius of holes is set to $r = 0.338a = 220$ nm. The thickness of the slab is set to $t = 0.461a = 300$ nm. The dashed box in Fig. 1(a) indicates the simulation area. All the simulations in our work are completed using the three-dimensional finite difference time domain (3D-FDTD) method.

The TE band diagram of the structure at the fundamental frequency is plotted in Fig. 1(b). The blue dots indicate the bulk bands while the red dots indicate the light line. The band-gap region is marked by a blue rectangle and the Brillouin zone used for the sweep is also plotted. According to previous work [9], the band edge mode at the upper bulk band near the band gap can be selected for the frequency conversion as shown in Fig. 1(b). The $|H_z|$ field of the chosen band-edge mode inside the brown circle in Fig. 1(b) is demonstrated in the left-hand side in Fig. 1(c). The absolute value is shown to search the position with the maximum energy. The TM band diagram of the structure at the second-harmonic frequency is plotted in the top part in Fig. 1(d). The $|E_z|$ field of the chosen BIC mode inside the black circle in Fig. 1(d) is demonstrated

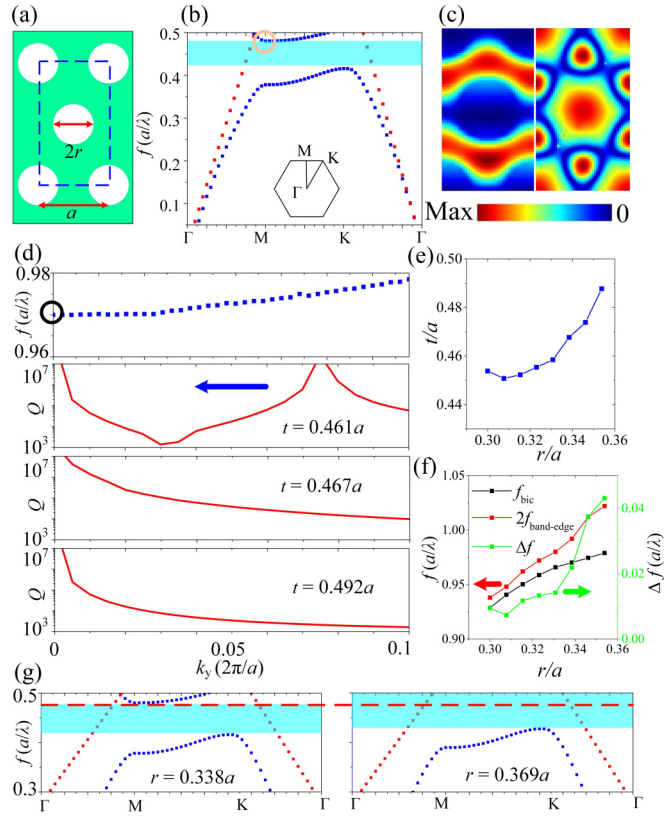

FIG. 1. (a) Schematic of the simulated LN unit cell with $r = 0.338a$ and $t = 0.461a$. (b) Band diagram at the fundamental frequency and the corresponding Brillouin zone, the band gap is marked by blue rectangle. (c) Field profiles of the modes inside the circles at fundamental and second-harmonic frequencies, the left figure of $|H_z|$ field is from the mode in brown circle in (b), while the right figure of $|E_z|$ field is from the mode in black circle in (d). (d) Band diagram at second-harmonic frequency together with the Q-factor variations of the band at the thicknesses of $t = 0.461a$, $0.467a$, and $0.492a$. (e) Variation of the thickness where the merged BIC locates versus the radii of holes. (f) Dependence of radius of the holes on the doubled frequency of the band-edge mode outside the light cone, the frequency of the merged BIC, and their difference, respectively. The frequencies difference cannot attain 0. (g) Band diagram at the fundamental frequency with $r = 0.338a$ and $r = 0.369a$. The band-edge mode in left figure locates at the band-gap region in right figure.

in the right-hand side of Fig. 1(c). From the field profiles it can be inferred that the energy in the chosen TE mode is mainly located in two side lobes around the hole, while the the energy in the chosen TM mode is mainly located in six clusters around the hole. The TM band indicates a symmetry-protected BIC and an accidental BIC, which is verified by calculating the Q factors of the band. The second part of Fig. 1(d) shows that at $k_y = 0$ and $k_y = 0.075$ $(2\pi/a)$ the Q factors become infinite when $t = 0.461a$. Previous work already demonstrated that the FDTD method can simulate above the 10^6 Q factor [9]. As for the TE band, the Q factor at the Γ point is infinite, owing to the fact that it locates outside the light cone. According to the conservation law of the topological charge, the accidental BIC mode will move

its position in k space as the thickness or the lattice constant of PhC gradually changes while the symmetry-protected BIC will be fixed [1,15]. Here the thickness of the slab is gradually increased and it can be observed that the accidental BIC mode gradually merges toward the Γ point and finally the merged BIC mode can be obtained at $t = 0.467a$ as shown in the third part in Fig. 1(d). The blue arrow indicates the moving direction as shown in Fig. 1(d). At the merged BIC point the Q factor decreases extremely slowly as k_y increases, which is the evidence of the merged BIC. As the thickness becomes larger, the topological charges will cancel each other and the mode at the Γ point will be a symmetry-protected BIC again instead of the merged BIC. The evolution of the Q factors is shown for a broader range of thicknesses (see the Supplemental Material [33]). Although the structure in Fig. 1(a) does not work near 1550 nm, according to the scaling rule of PhC, by changing the absolute value of the lattice constant the device can work near 1550 nm.

Next, the requirement of the mode-matching condition must be satisfied, i.e., $f_{\text{acc-BIC}} = 2f_{\text{band-edge}}$ must be satisfied. In the current geometry parameter, the mode-mismatch $\Delta f = f_{\text{acc-BIC}}\text{-}2f_{\text{band-edge}}$ still cannot attain zero. According to previous work [9], the mode-matching can be achieved by adjusting one geometry parameter like r or t as the $f_{\text{acc-BIC}}$ and $2f_{\text{band-edge}}$ change with different speeds versus r or t. However, once r or t is adjusted, the BIC will no longer be the merged state. Intuitively, both r and t can be varied for the mode-matching. Here the r is gradually varied, and according to the conservation law of the topological charge, for each r there must be a certain t where the merged BIC locates. In Fig. 1(e) we show the thicknesses of the slab where the merged BIC locate versus the numerous radii of holes. We show the evolution of the Q factors for different radius as the thickness changes (see the Supplemental Material [33]). Interestingly, as the radius decreases, the thickness attains a saturation value. Variations of $f_{\text{acc-BIC}}$, $2f_{\text{band-edge}}$ and Δf versus r are plotted in Fig. 1(f) and it should be noted that for each different r in the abscissa of Fig. 1(f) its corresponding t is also different to ensure each point is a state where BICs merge. As r decreases the Δf also attains a saturation value and cannot approach zero. The simulated results indicate that adjusting both r and t is not sufficient to realize the mode-matching condition.

In Fig. 1(g) the band diagram at the fundamental frequency for $r = 0.338a$ and $r = 0.369a$ are plotted. It can be seen that the whole bands have moved into the higher frequency when $r = 0.369a$. That is to say, the selected band with $r = 0.338a$ locates at the band-gap region in the diagram with $r = 0.369a$. Consequently, the PhC with larger r can be used to confine light at the fundamental frequency in our device.

To make the band-edge mode outside the light cone match the merged BIC mode, six new small holes around the large hole are added, as shown in Fig. 2(a). The implementation does not break the symmetry of the system and the merged topological charge at the Γ point will not suddenly disappear [35,36]. Constructing the supercell with the large and the small holes was already used to achieve BIC-based negative refraction [37]. Here the parameters are $a = 650$ nm, $t = 286$ nm, and $r_{c1} = 210$ nm, respectively. r_{c1} and r_{c2} represent the radius of the large holes and small holes. The

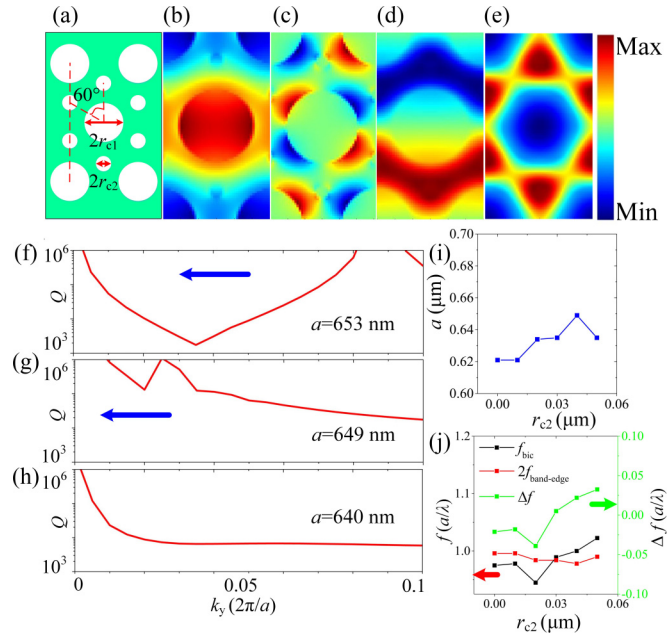

FIG. 2. (a) Schematic of the simulated LN unit cell with $a =$ 650 nm, $t = 0.44a$, and $r_{c1} = 0.323a$ and $r_{c2} = 0.076a$. (b) E_x, (c) E_y, and (d) H_z field profiles of the modes at the fundamental frequency and (e) E_z field profile at the second-harmonic frequency. (f)–(h) Q-factor variations of the band with the lattice constant of 653 nm, 649 nm, and 640 nm, respectively. (i) Variations of the lattice constant where the merged BIC locates versus radii of holes. (j) Dependence of radius of holes on the doubled frequency of the band-edge mode outside the light cone, the frequency of the merged BIC mode, and their difference, respectively. The frequencies' difference can attain 0.

mode profiles of the band-edge mode outside the light cone is shown in Figs. 2(b) to 2(d). The mode profile of the merged BIC at Γ point are shown in Fig. 2(e). Here the profiles are plotted to ensure the fundamental and the second-harmonic modes have a nonzero nonlinear overlapping factor. The principle of this design mainly lies in the different field distributions of the fundamental and the second-harmonic modes. We expect that adding small holes influences the wavelength of the BIC mode more than the band-edge mode owing to that the energy mainly distributes over the area where the small holes are constructed. As the a is gradually adjusted, the accidental BICs will merge at the Γ point and the merged BIC can be obtained. When $r_{c2} = 50$ nm, the Q-factor variations of the band at the lattice constant of 653 nm, 649 nm, and 640 nm versus k are plotted as shown in Figs. 2(f) to 2(h), respectively. The blue arrow indicates the moving direction of the accidental BIC. In comparison to the results in Fig. 1(d) the simulated maximum Q factor becomes lower. The reason lies in that adding a small structure enhances the difficulties of dividing the mesh and this does not reflect the descent of the actual Q factor. It reminds us that, for each lattice constant, we will select a suitable r_{c2} to achieve the mode-matching condition. In Fig. 2(i) the lattice constant variations of the slab where the merged BIC locates for numerous radii of small holes are shown. For each merged BIC point $f_{\text{acc-BIC}}$, $2f_{\text{band-edge}}$ and Δf versus r are shown in Fig. 2(j) and similarly

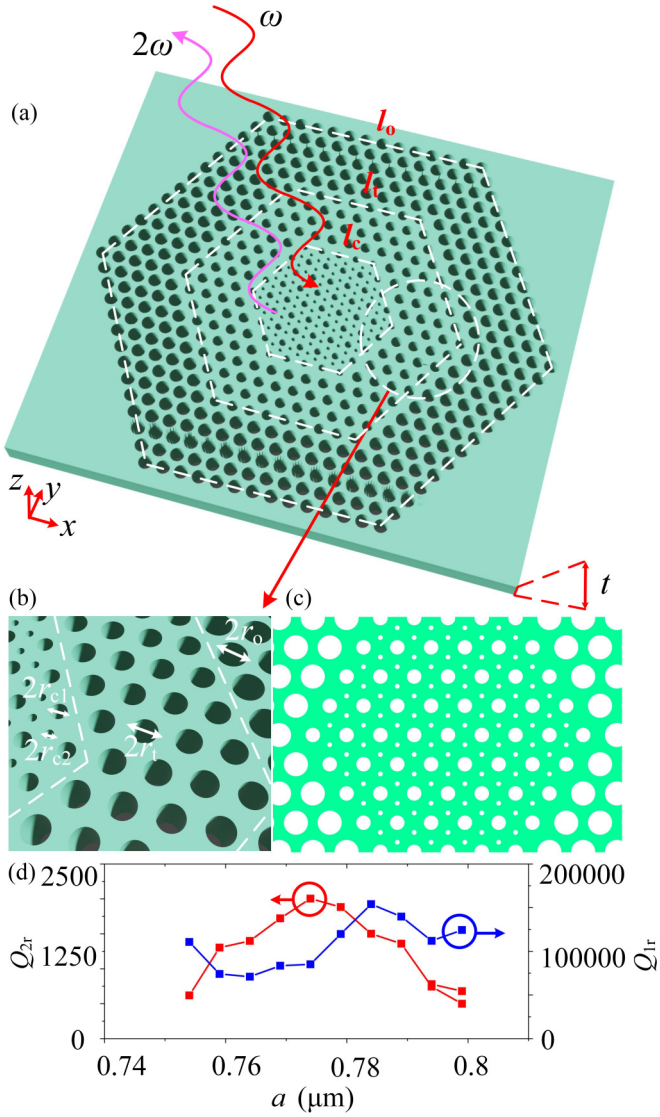

FIG. 3. (a) Model of simulated heterostructure PhC cavities with $r_{c1} = 254$ nm, $r_t = 260$ nm, $r_o = 270$ nm, and $r_{c2} = 30$ nm. (b) Three-dimensional and (c) two-dimensional enlarged views of the proposed device. (d) Dependence of radiative Q factors of the BIC mode and band-edge mode versus the lattice constants. For the BIC mode, the maximum Q factor of 2000 near merge state is about four times larger than the one in isolated state of 500. The Q factor of the band-edge mode oscillates between 80 000 and 160 000.

it should be noted that, for each different r_{c2} in the abscissa, its corresponding a is also different to ensure each point is a merged BIC point. As we predict the $2f_{\text{band-edge}}$ nearly stays steady as r_{c2} varies while the $f_{\text{acc-BIC}}$ changes fiercely. Δf finally crosses the zero point and the matching condition can be realized. The method of adding small holes can adjust the Δf over a large range.

III. RESULTS AND DISCUSSION

In this section, the heterostructure PhC cavity is considered as shown in Fig. 3(a). The lattice constant of the device is enlarged compared with that in Fig. 1 to ensure the cavity works near 1550 nm. The small and the large holes possess the same lattice constant. The optical axis of the material points to the z direction. Like previous work [9], the heterostructure PhC can be divided into the core region, transition region, and outer region. These regions possess the same lattice constant. The outer region is constructed for confining the photons near 1550 nm, like previous work [38], and the transition region is just for improving the Q factor [9]. The radii of the holes in the core, transition, and outer regions are $r_{c1} = 254$ nm, $r_t = 260$ nm, and $r_o = 270$ nm. By carefully adjusting the geometry parameters the mode-matching condition can be satisfied. The side lengths of the three regions are $l_c = 10a$, $l_t = 14a$, and $l_o = 24a$, respectively. Only in the core region are there small holes and $r_{c2} = 30$ nm. The thickness is $t = 345$ nm, which is fixed. When the lattice constant is $a = 769$ nm, the device supports the merged BIC mode at 796.79 nm and a band-edge mode at 1595.27 nm. These wavelengths can be adjusted by thermorefractive tuning [39].

In Fig. 3(d) the dependence of the radiative Q factor of the BIC mode and the band-edge mode on the lattice constant of the structure is plotted. When $a = 774$ nm, the Q factor obtains its maximum value of 2005, while for the isolated BIC it is below 1000. This is evidence of the merged BIC mode for a finite-size PhC [13]. The reason why the quality factor obtains its maximum value near the merging point was already explained in a previous work [13]. The difference of the Q factors between isolated and merged BIC is larger in PhC with high-refractive index material [13]. It should be noted that, when a becomes larger, the accidental BIC mode and the symmetry-protected BIC mode are separated while there are two Q factors for a fixed a. The Q factor of the band-edge mode oscillates over a small range of a.

To characterize the performance of the proposed device, the field profiles and the far-field emission profiles of the merged BIC mode and the band-edge mode outside the light cone are plotted. The $|E_z|$ field profile of the merged BIC mode is shown in Fig. 4(a). In Fig. 4(b) the polar far-field emission profiles of the merged BIC mode in the upper half space are obtained. In Figs. 4(c) the $|H_z|$ field of the fundamental band-edge mode is plotted. In Fig. 4(d) the far-field emission profiles of the band-edge mode in the upper half space are obtained. The results indicate that both far-field emissions are highly collimated around the normal incidence, which leads to efficient excitation and collection of the nonlinear signal [9].

At last we estimate the performance of the proposed device as a nonlinear cavity. The second-harmonic generation efficiency can be calculated using the formula [9,11,40]

$$\frac{P_o}{P_i^2} = \frac{8}{\omega_1}\left(\frac{\chi^{(2)}}{\sqrt{\epsilon_0 \lambda_{FH}^3}}\right)^2 |\overline{\beta}|^2 Q_{FH}^2 Q_{SH}, \tag{1}$$

where ϵ_0 is the vacuum permittivity. $\overline{\beta}$ can be determined by [9,11,41]

$$\overline{\beta} = \frac{\int d\mathbf{r} \sum_{ijk} \overline{\chi}_{ijk} E_{2\omega i}^* E_{\omega j} E_{\omega k}}{(\int d\mathbf{r} \epsilon_\omega(\mathbf{r}) |\mathbf{E}_\omega|^2)(\int d\mathbf{r} \epsilon_{2\omega}(\mathbf{r}) |\mathbf{E}_{2\omega}|^2)^{1/2}} \lambda_{FH}^{3/2}, \tag{2}$$

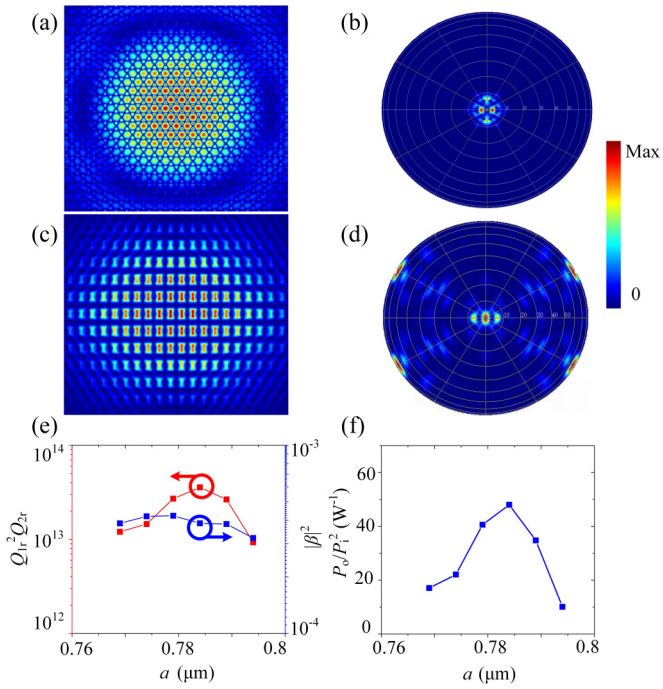

FIG. 4. Field profiles of the modes at (a) 796.79 nm. Polar far-field emission profiles of the modes at (b) 796.79 nm. Field profiles of the modes at (c) 1595.27 nm. Polar far-field emission profiles of the modes at (d) 1595.27 nm. (e) The $Q_{1r}^2 Q_{2r}$ and square of nonlinear overlapping factors versus lattice constants. (f) Second harmonic generation efficiency versus lattice constants. The maximum efficiency of 48 W^{-1} is four times larger than the one of minimum value 10 W^{-1}.

where λ_{FH} is the wavelength of the band-edge mode, $\overline{\chi_{ijk}}$ is the dimensionless nonlinear tensor elements. We analyze the factors which influence the conversion efficiency (see the Supplemental Material [33]). Here we assume that the extrinsic Q factor is infinite and the perfect pumping and collecting condition can be satisfied. We note that most energy is distributed in the center of the cavity and the electric field data in the boundary of the cavity are not considered for convenience of calculation. Consequently, the $|\overline{\beta}|$ is a little larger than its actual value, but it does not influence its relative value for different lattice constants.

It can be inferred that the theoretical second-harmonic generation efficiency is mainly determined by the Q factors at the fundamental and the second harmonic frequencies and the nonlinear overlapping factor. In our work, the PhC slab is constructed by LN and the optical axis is pointed to a fixed direction. The resonant frequencies of modes at different constants near 784 nm are similar. In Fig. 4(e) we demonstrate the product of, the square of the Q factor of the band-edge mode, and the Q factor of the BIC mode versus lattice constants. The square of the nonlinear overlapping factors versus lattice constants is also shown. The results indicate that $Q_{FH}^2 Q_{SH}$ also show a peak near the merged BIC point and the square of β is steady over the lattice constants we focus on. Consequently, the second-harmonic generation efficiency will obtain its maximum value near the merged BIC point as shown in Fig. 4(f). The maximum value is 48 W^{-1} (4800% W^{-1}). The value is far larger than that of isolated BIC (10 W^{-1}).

IV. CONCLUSION

In conclusion, we proposed a doubly resonant LN PhC cavity using the merged BIC to achieve a higher SHG efficiency. The unit cell of large and small holes is established and a band-edge mode at the fundamental frequency will be matched with the merged BIC mode. It can be found that the SHG of the merged BIC of 48 W^{-1} (4800% W^{-1}) is higher than the one of the isolated BIC. Our design recipe is not limited to LN and can be extended to other nonlinear materials like GaN or AlGaAs. In addition, except for the second-harmonic generation, our design can apply to the parametric down-conversion process. Except for the higher Q factor at the merged BIC point for a finite-size PhC, the merit of the merged BIC also includes the robustness of the Q factor against the random fluctuations on radii or lattice constants of the holes. Consequently, the nonlinear conversion efficiency may show slighter degradation compared with the one of isolated BIC against disorder. However, it is just a hypothesis and requires our future simulation to verify. The introduction of small holes at critical positions without breaking the symmetry may help the mode-matching process, which may benefit the design of the triple resonant cavity for more colorful nonlinear processes. This work is expected to broaden the application of the merged BIC in the nonlinear photonic area.

ACKNOWLEDGMENTS

This work was supported by the National Natural Science Foundation of China (Grants No. 91950107 and No. 12134009), the National Key R&D Program of China (Grant No. 2019YFB2203501), Shanghai Municipal Science and Technology Major Project (Grant No. 2019SHZDZX01-ZX06), and SJTU Grant No. 21X010200828.

[1] B. Zhen, C. W. Hsu, L. Lu, A. D. Stone, and M. Soljačić, Topological Nature of Optical Bound States in the Continuum, Phys. Rev. Lett. **113**, 257401 (2014).

[2] C. Huang, C. Zhang, S. Xiao, Y. Wang, Y. Fan, Y. Liu, N. Zhang, G. Qu, H. Ji, J. Han *et al.*, Ultrafast control of vortex microlasers, Science **367**, 1018 (2020).

[3] X. Wang, J. Xin, Q. Ren, H. Cai, J. Han, C. Tian, P. Zhang, L. Jiang, Z. Lan, J. You *et al.*, Plasmon hybridization induced by quasi bound state in the continuum of graphene metasurfaces oriented for high-accuracy polarization-insensitive two-dimensional sensors, Chin. Opt. Lett. **20**, 042201 (2022).

[4] S. Liu, H. Tong, and K. Fang, Optomechanical crystal with bound states in the continuum, Nat. Commun. **13**, 3187 (2022).

[5] S. D. Krasikov, A. A. Bogdanov, and I. V. Iorsh, Nonlinear bound states in the continuum of a one-dimensional photonic crystal slab, Phys. Rev. B **97**, 224309 (2018).

[6] X. Zhang, Y. Liu, J. Han, Y. Kivshar, and Q. Song, Chiral emission from resonant metasurfaces, Science **377**, 1215 (2022).

[7] X. Yin, J. Jin, M. Soljačić, C. Peng, and B. Zhen, Observation of topologically enabled unidirectional guided resonances, Nature (London) **580**, 467 (2020).

[8] Y. Zeng, G. Hu, K. Liu, Z. Tang, and C.-W. Qiu, Dynamics of Topological Polarization Singularity in Momentum Space, Phys. Rev. Lett. **127**, 176101 (2021).

[9] M. Minkov, D. Gerace, and S. Fan, Doubly resonant χ (2) nonlinear photonic crystal cavity based on a bound state in the continuum, Optica **6**, 1039 (2019).

[10] J. Wang, M. Clementi, M. Minkov, A. Barone, J.-F. Carlin, N. Grandjean, D. Gerace, S. Fan, M. Galli, and R. Houdré, Doubly resonant second-harmonic generation of a vortex beam from a bound state in the continuum, Optica **7**, 1126 (2020).

[11] S. Zanotti, M. Minkov, S. Fan, L. C. Andreani, and D. Gerace, Doubly-resonant photonic crystal cavities for efficient second-harmonic generation in iii–v semiconductors, Nanomaterials **11**, 605 (2021).

[12] J. Jin, X. Yin, L. Ni, M. Soljačić, B. Zhen, and C. Peng, Topologically enabled ultrahigh-q guided resonances robust to out-of-plane scattering, Nature (London) **574**, 501 (2019).

[13] M.-S. Hwang, H.-C. Lee, K.-H. Kim, K.-Y. Jeong, S.-H. Kwon, K. Koshelev, Y. Kivshar, and H.-G. Park, Ultralow-threshold laser using super-bound states in the continuum, Nat. Commun. **12**, 1 (2021).

[14] M. Kang, S. Zhang, M. Xiao, and H. Xu, Merging Bound States in the Continuum at Off-High Symmetry Points, Phys. Rev. Lett. **126**, 117402 (2021).

[15] M. Kang, L. Mao, S. Zhang, M. Xiao, H. Xu, and C. T. Chan, Merging bound states in the continuum by harnessing higher-order topological charges, Light Sci. Appl. **11**, 228 (2022).

[16] C. Zhao, W. Chen, J. Wei, W. Deng, Y. Yan, Y. Zhang, and C.-W. Qiu, Electrically tunable and robust bound states in the continuum enabled by 2D transition metal dichalcogenide, Adv. Opt. Mater. **10**, 2201634 (2022).

[17] S. Wan, K. Wang, F. Wang, C. Guan, W. Li, J. Liu, A. Bogdanov, A. Belov, and P J. Shi, Topologically enabled ultrahigh-q chiroptical resonances by merging bound states in the continuum, Opt. Lett. **47**, 3291 (2022).

[18] H. Barkaoui, K. Du, Y. Chen, S. Xiao, and Q. Song, Merged bound states in the continuum for giant superchiral field and chiral mode splitting, Phys. Rev. B **107**, 045305 (2023).

[19] L. Huang, B. Jia, Y. K. Chiang, S. Huang, C. Shen, F. Deng, T. Yang, D. Powell, Y. Li, and A. Miroshnichenko, Topological supercavity resonances in the finite system, Adv. Sci. **9**, 2200257 (2022).

[20] L. Kang, H. Bao, and D. H. Werner, Efficient second-harmonic generation in high q-factor asymmetric lithium niobate metasurfaces, Opt. Lett. **46**, 633 (2021).

[21] F. Ye, Y. Yu, X. Xi, and X. Sun, Second-harmonic generation in etchless lithium niobate nanophotonic waveguides with bound states in the continuum, Laser Photonics Rev. **16**, 2100429 (2022).

[22] X. Zhang, L. He, X. Gan, X. Huang, Y. Du, Z. Zhai, Z. Li, Y. Zheng, X. Chen, Y. Cai *et al.*, Quasi-bound states in the continuum enhanced second-harmonic generation in thin-film lithium niobate, Laser Photonics Rev. **16**, 2200031 (2022).

[23] Z. Huang, K. Luo, Z. Feng, Z. Zhang, Y. Li, W. Qiu, H. Guan, Y. Xu, X. Li, and H. Lu, Resonant enhancement of second harmonic generation in etchless thin film lithium niobate heteronanostructure, Sci. China Phys. Mech. Astron. **65**, 104211 (2022).

[24] Z. Zheng, L. Xu, L. Huang, D. Smirnova, P. Hong, C. Ying, and M. Rahmani, Boosting second-harmonic generation in the linbo 3 metasurface using high-q guided resonances and bound states in the continuum, Phys. Rev. B **106**, 125411 (2022).

[25] S. Duan, Y. Chen, G. Li, C. Zhu, and X. Chen, Broadband polarization beam splitter based on a negative refractive lithium niobate photonic crystal slab, Chin. Opt. Lett. **14**, 042301 (2016).

[26] H. Jiang, H. Liang, R. Luo, X. Chen, Y. Chen, and Q. Lin, Nonlinear frequency conversion in one dimensional lithium niobate photonic crystal nanocavities, Appl. Phys. Lett. **113**, 021104 (2018).

[27] R. Ge, X. Yan, Z. Liang, H. Li, J. Wu, X. Liu, Y. Chen, and X. Chen, Large quality factor enhancement based on cascaded uniform lithium niobate bichromatic photonic crystal cavities, Opt. Lett. **48**, 113 (2023).

[28] C. Lu, B. Zhu, C. Zhu, L. Ge, Y. Liu, Y. Chen, and X. Chen, All-optical logic gates and a half-adder based on lithium niobate photonic crystal micro-cavities, Chin. Opt. Lett. **17**, 072301 (2019).

[29] R. Ge, X. Yan, Y. Chen, and X. Chen, Broadband and lossless lithium niobate valley photonic crystal waveguide, Chin. Opt. Lett. **19**, 060014 (2021).

[30] H. Liang, R. Luo, Y. He, H. Jiang, and Q. Lin, High-quality lithium niobate photonic crystal nanocavities, Optica **4**, 1251 (2017).

[31] M. Li, H. Liang, R. Luo, Y. He, and Q. Lin, High-q 2D lithium niobate photonic crystal slab nanoresonators, Laser Photonics Rev. **13**, 1800228 (2019).

[32] M. Li, H. Liang, R. Luo, Y. He, J. Ling, and Q. Lin, Photon-level tuning of photonic nanocavities, Optica **6**, 860 (2019).

[33] See Supplemental Material at http://link.aps.org/supplemental/10.1103/PhysRevB.107.165406 for further details about the utilization of the other tensor, the evolution of the quality factors during the merging process, and the mechanism of the improved conversion efficiency.

[34] S. Saravi, S. Diziain, M. Zilk, F. Setzpfandt, and T. Pertsch, Phase-matched second-harmonic generation in slow-light photonic crystal waveguides, Phys. Rev. A **92**, 063821 (2015).

[35] T. Yoda and M. Notomi, Generation and Annihilation of Topologically Protected Bound States in the Continuum and Circularly Polarized States by Symmetry Breaking, Phys. Rev. Lett. **125**, 053902 (2020).

[36] R. Chai, W. Liu, Z. Li, H. Cheng, J. Tian, and S. Chen, Multiband quasibound states in the continuum engineered by space-group-invariant metasurfaces, Phys. Rev. B **104**, 075149 (2021).

[37] L. Vertchenko, C. DeVault, R. Malureanu, E. Mazur, and A. Lavrinenko, Near-zero index photonic crystals with directive bound states in the continuum, Laser Photonics Rev. **15**, 2000559 (2021).

[38] Z. Chen, X. Yin, J. Jin, Z. Zheng, Z. Zhang, F. Wang, L. He, B. Zhen, and C. Peng, Observation of miniaturized bound states in the continuum with ultra-high quality factors, Sci. Bull. **67**, 359 (2022).

[39] G. Marty, S. Combrié, F. Raineri, and A. De Rossi, Photonic crystal optical parametric oscillator, Nat. Photonics **15**, 53 (2021).

[40] P. Hong, L. Xu, and M. Rahmani, Dual bound states in the continuum enhanced second harmonic generation with transition metal dichalcogenides monolayer, Opto-Electronic Advances **5**, 200097 (2022).

[41] Y. Chen, Z. Lan, J. Li, and J. Zhu, Topologically protected second harmonic generation via doubly resonant high-order photonic modes, Phys. Rev. B **104**, 155421 (2021).